Int. J. Electrochem. Sci., 15 **(2020)** 4203 – 4217, doi: 10.20964/2020.05.62

International Journal of
ELECTROCHEMICAL
SCIENCE
www.electrochemsci.org

A fluorine-doped $MnFe_2O_4$ nanorod/carbon composite as an anode material for high-performance lithium-ion batteries

Zihui Deng, Miao He, Yefeng Feng, Deping Xiong*

School of Physics and Optoelectronic Engineering, Guangdong University of Technology, Guangzhou 510006, China
*E-mail: herofate@126.com

Received: 4 Janaury 2020 / *Accepted:* 17 February 2020 / *Published:* 10 April 2020

A fluorine-doped $MnFe_2O_4$ nanorod and carbon nanocomposite (nanorod-$MnFe_2O_4$/F@C) is synthesized through a convenient and facile two-step hydrothermal method combined with a pyrolysis method. X-ray powder diffraction, Raman spectroscopy, a thermogravimetric analysis, scanning electron microscopy, transmission electron microscopy and X-ray photoelectron spectroscopy were utilized to investigate the structure, morphology and composition of the as-prepared samples. The as-synthesized anode material shows a superior rate performance (~ 490 mA h g^{-1} at a current density of 1 A g^{-1}), excellent cycling stability (~ 96% compared with the 2nd cycle) and enhanced discharge capacity (~ 900 mA h g^{-1} at a current density of 200 mA g^{-1} after 150 cycles) when compared with those of their counterparts. The excellent rate performance and superior cycling stability may be due to the doped fluorine, which can enhance electron and ion transport and suppress the decomposition of the electrolyte; additionally, the doped fluorine can promote the subsequent formation of a solid electrolyte interphase (SEI) film. Furthermore, the combination with carbon to produce an anode material can accommodate severe volume variations, provide good electrical contact, and improve conductivity in which all of the above can significantly enhance the electrochemical performance of $MnFe_2O_4$. The results suggest that nanorod-$MnFe_2O_4$/F@C is a promising anode material for lithium-ion batteries.

Keywords: Li-ion batteries; Anode materials; Energy storage and conversion; $MnFe_2O_4$; Fluorine doping.

1. INTRODUCTION

Large-scale exploitation of fossil fuels can cause serious environmental problems and air pollution. Therefore, the replacement of fossil fuels with clean and renewable energy is necessary and urgent. Since Sony first successfully developed ~~a~~ commercial lithium-ion batteries (LIBs) in 1992, they have been widely used as a kind of energy conversion and storage device in a variety of fields, ranging from portable electronics to electric vehicles (EVs) or hybrid EVs (HEVs); the reason for their use is their high energy storage density, efficiency, low cost, long cycling life and environmental friendliness [1-3]. At present, graphite is widely utilized as an anode material for commercial lithium-ion batteries owing to its resource abundance, low cost, long cycling life and nontoxicity. However, the theoretical specific capacity of graphite is only 372 mAh g^{-1} (corresponding to LiC_6). In addition, the growth of dendritic lithium on the anode surface during subsequent discharge-recharge cycles will penetrate the separator and produce a risk of causing a short circuit between the anode and cathode, which may lead to a battery explosion [4-6]. With the ever-increasing demand for developing high energy density and safe LIBs, there is an urgent demand for developing a novel anode material to overcome the shortcomings of commercial graphite.

Nanostructured transition metal oxides (TMOs) as anode materials for LIBs have been the most widely studied over the last several years because of their larger lithium storage capacities and increased safety compared to that of commercially used graphite [7]. Among the various TMOs (such as Fe_2O_3 [8, 9], Co_3O_4 [10, 11], MnO_2 [12, 13], and SiO_2 [14-16]), nanostructured iron-based mixed transition-metal oxides (MTMOs) with an AB_2O_4 cubic spinel crystal structure (A,B = Fe, Zn, Mn and so on), especially ferrites [17] (MFe_2O_4, M=Co [18-20], Zn [21-23], Mn [24-27]), have been explored as anode materials in LIBs due to their high theoretical capacity, resource abundance, and environmental friendliness. Compared with simple TMOs, MTMOs usually show superior electrochemical performance due to their complex chemical compositions that contain two transition elements, which provide an approach for adjusting the working voltage and energy density [28]; furthermore, MTMOs provide inherent synergistic effects between the two transition metal oxides in the lithium ion charge/discharge process between the two transition metal oxides [29]. Among these MTMO anodes, $MnFe_2O_4$ draws more attention owing to its high safety and low cost along with its high theoretical capacity of 930 mA h g^{-1} according to a redox reaction involving eight lithium ions per formula unit of $MnFe_2O_4$ [30]. However, some challenges still have to be solved in the $MnFe_2O_4$ anode material. $MnFe_2O_4$ shows a rapid capacity decrease during cycling and high charge/discharge rates due to a large volume change that occurs with electrodes prepared with nanoscaled anode material [21], along with the poor electron and ion conductivity of $MnFe_2O_4$ [24]. To overcome these problems, incorporating $MnFe_2O_4$ with carbonaceous materials is considered to be an effective strategy. Carbon has high electrical conductivity, and the volume variation during Li-ion insertion/extraction is much smaller than that of transition metal oxides. [31-34]. On the other hand, both theoretical and experimental studies confirm that the introduction of heteroatoms such as N^{3-}, S^{2-}, Cl^-, and F^-, which partially replace some of the oxygen, can effectively reduce lattice change and impedance; the above replacements lead to significantly improved electrochemical performance, such as a high discharge capacity, superior cycling stability and an excellent rate performance compared with that of a non-doped counterpart [35-39]. Fluorine has a similar ionic radius compared with that of oxygen and is the most suitable anion dopant due to its lower lattice deformation compared with that of other alternatives. Furthermore, the presence of fluoride can suppress the decomposition of the electrolyte, which leads to the formation of a thick solid electrolyte interphase (SEI) film, and eventually, the cycling stability of the anode material is enhanced [40].

In this paper, fluorine-doped $MnFe_2O_4$ nanorods and carbon nanocomposites (nanorod-$MnFe_2O_4$/F@C) are synthesized using a facile and convenient hydrothermal route by employing ammonium fluoride as the fluorine source with a subsequent annealing treatment. The nanorod-

$MnFe_2O_4/F@C$ is obtained by drying and in-situ carbonization of a sucrose coating on the surface of the fluorine-doped $MnFe_2O_4$ nanorods (nanorod-$MnFe_2O_4/F$) by the pyrolysis of sucrose in the subsequent annealing process. The unique structure is expected to provide superior electrochemical performance because of its improved electronic conductivity, along with an improved Li-ion diffusion speed and path; additionally, the structure provides an elastic buffer layer to accommodate the volume variation of the material during the Li-ion insertion and extraction processes. The as-synthesized nanorod-$MnFe_2O_4/F@C$ exhibits a higher reversible discharge capacity, better rate performance and superior cycling stability compared to that of $MnFe_2O_4$ nanorods and carbon nanocomposites (nanorod-$MnFe_2O_4@C$).

2. EXPERIMENTAL

2.1 Materials preparation

2.1.1 Synthesis of nanorod-$MnFe_2O_4/F$

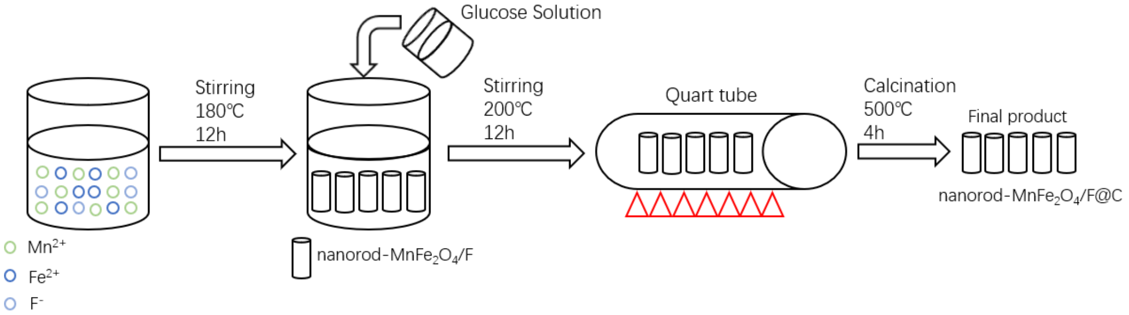

Figure 1. Schematic diagram showing the preparation process of nanorod-$MnFe_2O_4/F@C$.

The synthesis process of nanorod-$MnFe_2O_4/F$ via a hydrothermal reaction is illustrated in Fig. 1. A typical synthesis procedure of the nanorod-$MnFe_2O_4/F$ nanocomposite is as follows: First, 1.2 mmol manganese acetate tetrahydrate ($Mn(CH_3COO)_2\cdot 4H2O$) and 2.4 mmol iron chloride hexahydrate ($FeCl_3\cdot 6H_2O$) were mixed and dissolved in a 100-ml mixed solution of deionized (DI) water and absolute ethanol (1:1 in volume ratio) with sonication to form a uniform solution. Then, 10 mmol urea, 10 mmol NH_4F and 12 mmol KCl were added to the above solution. After stirring for several hours to form a homogeneous solution, the solution was transferred to a Teflon-lined stainless steel autoclave (100-mL ~~in~~ capacity) and then heated in an electric oven at 180 °C for 12 h. After cooling to room temperature, the resulting product was collected by centrifugation, washed with DI water and absolute ethanol ~~for~~ several times and dried at 60 °C overnight. The synthesis of the $MnFe_2O_4$ nanorods (nanorod-$MnFe_2O_4$) was similar to that of nanorod-$MnFe_2O_4/F$ but without the addition of NH_4F.

2.1.2 Synthesis of nanorod-$MnFe_2O_4$/F@C

The synthesis process of nanorod-$MnFe_2O_4$/F@C is also illustrated in Fig. 1. First, 200 mg nanorod-$MnFe_2O_4$/F was dispersed in 25 ml DI water by ultrasonication to form a suspension. Then, 500 mg glucose ($C_6H_{12}O_6{\cdot}3H_2O$) was dissolved in the above solution with stirring for 30 min. The resulting suspension was transferred to a 40-mL Teflon autoclave and heated in an electric oven at 200 °C for 12 h. After cooling to room temperature, the resulting product was collected by centrifugation, washed with DI water and absolute ethanol several times and dried at 60 °C overnight. The resulting product was annealed in a tube furnace for 4 h in a N_2 atmosphere with a heating rate of 5 °C min^{-1} to a final temperature of 500 °C. The synthesis of nanorod-$MnFe_2O_4$@C was similar to that of nanorod-$MnFe_2O_4$/F@C but without the addition of NH_4F.

2.2 Materials characterization

The X-ray diffraction (XRD) patterns of the samples were obtained by a Bruker D8-advance powder diffractometer with ~~a~~ Cu Kα radiation (λ= 1.54182 Å). X-ray photoelectron spectroscopy (XPS) was carried out on a Thermo Scientific Escalab 250Xi equipped with a non-monochromatic Mg-Kα X-ray source at 1486.6 eV to analyse the chemical composition of the products on the surface. The carbon content in the composite was measured by a thermogravimetric analysis (TGA, TA Q500) in an air flow from room temperature to 800 °C at a heating rate of 10 °C min^{-1}. Raman spectra were measured on a Renishaw Raman system 2000 using a 514 nm argon-ion laser as an excitation source. Field-emission transmission electron microscopy (FETEM), high-resolution TEM (HRTEM) analysis and selected area electron diffraction (SAED) patterns were obtained on an FEI Tecnai G2 20 with an accelerating voltage of 200 kV. Field-emission scanning electron microscopy (FESEM, Hitachi S-3400N) equipped with energy-dispersive X-ray spectroscopy (EDS) was performed with an accelerating voltage of 15 kV to observe and analyse the microstructure and morphology of the products.

2.3 Electrochemical measurements

The working electrode was fabricated by mixing and dissolving 70 wt% active materials, 15 wt% conductive carbon (acetylene black), and 15 wt% polyvinylidene fluoride (PVDF) in N-methyl-2-pyrrolidione (NMP) to produce a homogeneous slurry, which was followed by coating onto a copper foil with a blade. Subsequently, the working electrode was dried in a vacuum oven at 80 °C for 12 h. Then, the copper foil was pressed and punched into discs for use as the working electrode. Subsequently, coin-type half-cells (CR2032) were assembled in an argon-filled glove box (Etelux LAB2000) with an oxygen and a water content of less than 1 ppm, using lithium foil as the counter electrode, a Celgard 2400 polypropylene membrane as the separator, and a mixture of 1.0 mol L^{-1} $LiPF_6$ in ethylene carbonate (EC), diethyl carbonate (DEC), and dimethyl carbonate (DMC) (1:1:1 ~~in~~ volume ratio) as the electrolyte.

Galvanostatic charge/discharge tests were performed on a LAND BT2013A battery testing system at various current densities in a voltage range of 0.1-3.0 V. Cyclic voltammetry (CV) measurements were performed on an electrochemical workstation (CHI660E). CV measurements were obtained at a scan rate of 0.1 mV s^{-1} in a range of 0.01 V and 3 V (vs. Li/Li^+). All electrochemical tests were carried out at room temperature.

3. RESULTS AND DISCUSSION

Fig. 2a shows the XRD patterns of the obtained nanorod-$MnFe_2O_4$@C and nanorod-$MnFe_2O_4$/F@C. All the diffraction peaks are well indexed to standard cubic spinel-type $MnFe_2O_4$ (JCPDS No. 74-2403), and no obvious impurity phase is observed, indicating that the carbonization of glucoses does not change the crystal structure of nanorod-$MnFe_2O_4$@C and nanorod-$MnFe_2O_4$/F@C [41]. However, no diffraction peak corresponding to the crystalline phase of carbon materials is observed, suggesting that the carbon phase is amorphous [42, 43].

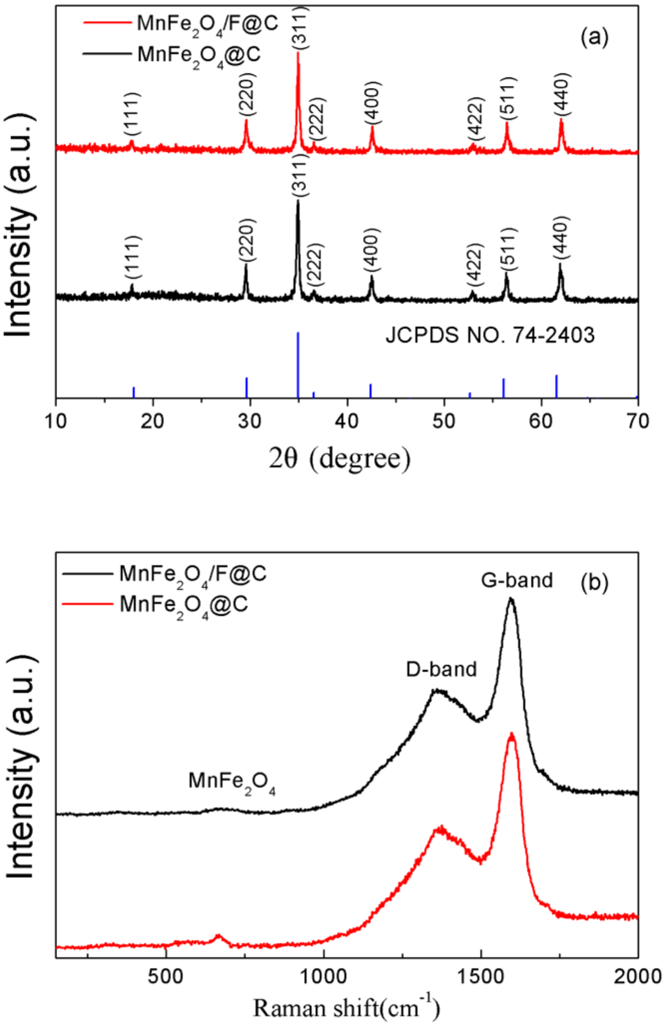

Figure 2. XRD patterns (a) and Raman spectra (b) of nanorod-$MnFe_2O_4$@C and nanorod-$MnFe_2O_4$/F@C.

It is noted that fluorine doping does not severely influence the peak positions of samples, which is attributed to the ionic radius of F^- being similar to O^{2-} [37]. The sharp diffraction peaks suggest the crystalline nature of the samples. The average lattice constant ~~*a*~~ of nanorod-$MnFe_2O_4$@C is 0.8506 nm, which is in good agreement with the 0.8511 nm of the standard cubic spinel-type $MnFe_2O_4$ (JCPDS No. 74-2403). However, the average lattice constant of nanorod-$MnFe_2O_4$/F@C becomes larger than nanorod-$MnFe_2O_4$@C and standard $MnFe_2O_4$ (JCPDS No. 74-2403). The reason for the different average lattice constants is that smaller oxygen ions are replaced by larger fluorine ions [35]. The average crystallite size of nanorod-$MnFe_2O_4$@C and nanorod-$MnFe_2O_4$/F@C can be estimated from Scherrer′s equation to be approximately 35 nm. Fig. 2b shows the Raman spectra of nanorod-$MnFe_2O_4$/F@C and nanorod-$MnFe_2O_4$@C. Two broad peaks located at 1359 and 1593 cm^{-1} are observed, proving the existence of carbon and corresponding to the D and G bands of the carbon coating, respectively [44, 45]. A weak peak at 600 cm^{-1} can be attributed to the vibration of $MnFe_2O_4$ nanoparticles [46]. The D band usually results from sp^3 carbon with disordered carbon originating from structural defects in the graphite crystals, while the G band results from orderly sp^2 carbon atoms in carbon rings or long carbon chains [47]. The peak intensity ratio between the D and G bands can be used as an indicator to estimate the degree of disorder and order in carbon material [48]. Apparently, the peak intensity of the D band is weaker than that of the G band, indicating a relatively high degree of graphitic structure. The higher graphitization degree of carbon is probably attributed to iron, which acts as an active catalyst for the formation of graphitic carbon [49] and is beneficial for improving the electron and ion conductivity of the material; thus, the presence of iron can enhance the electrochemical performance of the material [50].

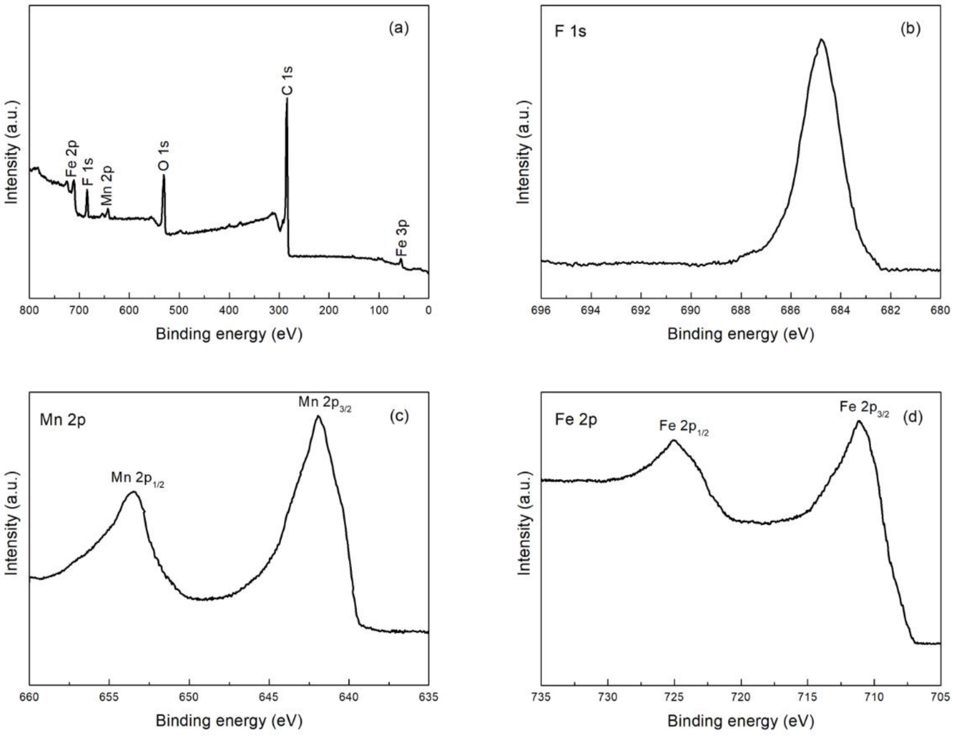

Figure 3. XPS spectra of nanorod-$MnFe_2O_4$/F@C: (a) survey scan, (b) F 1s spectrum, (c) Mn 2p spectrum, and (d) Fe 2p spectrum.

The chemical composition and valence state of nanorod-$MnFe_2O_4$/F@C was investigated by an XPS analysis. Fig. 3a reveals the survey scan of nanorod-$MnFe_2O_4$/F@C, showing the existence of only Mn, Fe, F, O, and C elements. Fig. 3b shows the F 1s spectrum. A strong peak is located at 685 eV, which is in close agreement with that of other reports [38, 51, 52]; thus, the F 1s spectrum confirms that fluorine is successfully doped into the $MnFe_2O_4$ lattice. In Fig. 3c, the Mn 2p spectrum exhibits two characteristic peaks at 641 and 653 eV, corresponding to Mn $2p_{1/2}$ and Mn $2p_{3/2}$, respectively, which is consistent with the typical characteristic peaks of Mn^{2+} [53, 54]. Fig. 3d shows the Fe 2p spectrum. The two characteristic peaks located at 711 and 724 eV can be attributed to ~~the~~ Fe $2p_{3/2}$ and Fe $2p_{1/2}$, respectively, which is consistent with the peak of Fe^{3+} reported previously [55, 56].

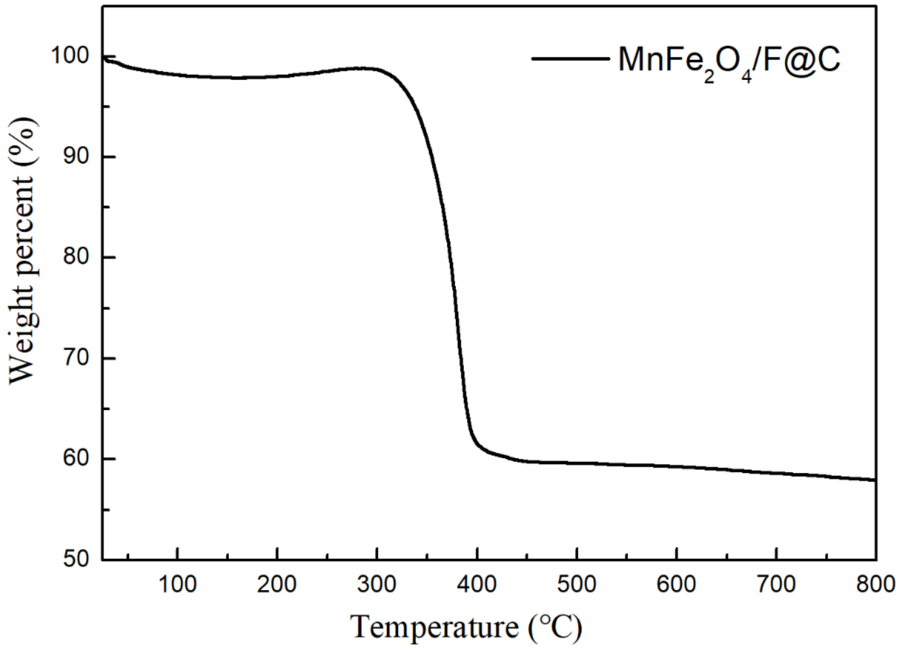

Figure 4. TGA curves of nanorod-$MnFe_2O_4$/F@C

The carbon content of the as-synthesized nanorod-$MnFe_2O_4$/F@C was evaluated by a TGA curve in an air atmosphere, as shown in Fig. 4. The weight loss below 100 °C is due to the evaporation of physically adsorbed water. Then, a slight weight increase from 150 to 250 °C corresponds to the preoxidation reaction of carbon on carbon shells [27]. The rapid weight loss between 300 °C and 400 °C can be ascribed to the oxidation of carbon in air. The carbon content of nanorod-$MnFe_2O_4$/F@C is estimated to be approximately 38.2 wt%. Therefore, the content of nanorod-$MnFe_2O_4$/F in nanorod-$MnFe_2O_4$/F@C can be estimated to be approximately 61.8 wt%.

Fig. 5a, b shows the low-magnification SEM image of the nanorod-$MnFe_2O_4$/F@C with a mean diameter of 120 nm and lengths ranging from 200 nm to 600 nm. It can be clearly seen that the $MnFe_2O_4$ nanorods are well dispersed and mixed with the carbon matrix. In these nanocomposites, the $MnFe_2O_4$ nanorods provide a large specific surface area, which leads to relatively short Li ion and electron diffusion pathways and provides more active sites for Li-ion storage; thus, the nanorods can enhance the kinetics of Li ions and electrons. Moreover, the carbon coating improves the electrochemical performance of $MnFe_2O_4$ nanorods by suppressing the aggregation of nanorods and alleviating the drastic volume variation during Li-ion insert/extraction.

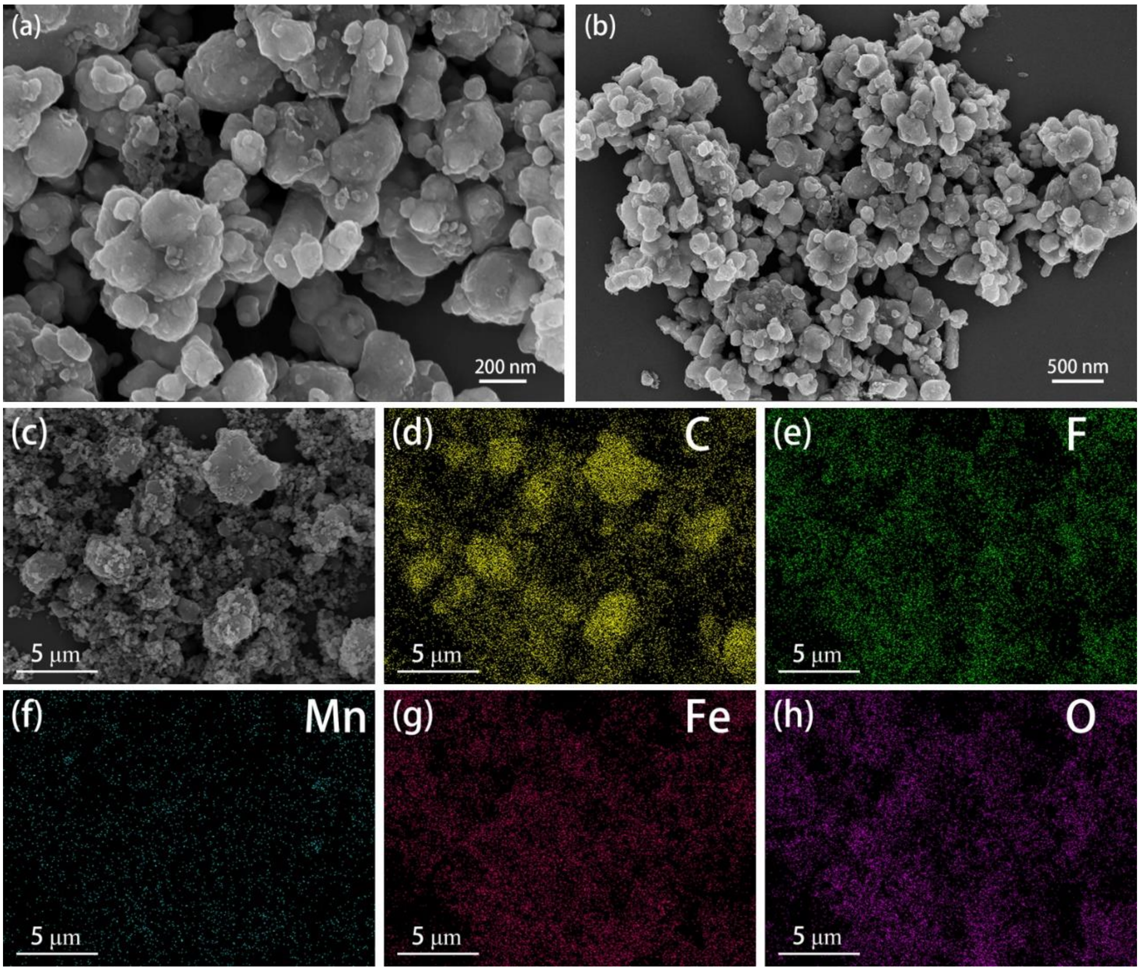

Figure 5. (a, b) SEM images of nanorod-$MnFe_2O_4$/F@C. (c) SEM images of nanorod-$MnFe_2O_4$/F@C and its corresponding elemental mapping images: (d) C, (e) F, (f) Mn, (g) Fe, and (h) O.

On the other hand, the carbon matrix in the composite improves the electrical conductivity and forms a stable SEI film to maintain the structural integrity. As a result, with such a structure, the as-synthesized sample can have potential applications as an anode material for lithium-ion batteries. To investigate the elemental distribution on the nanorod-$MnFe_2O_4$/F@C, an SEM image and the corresponding EDS elemental mapping of C, F, Mn, Fe and O elements are shown in Fig. 5c-h. EDS elemental mapping shows that nanorod-$MnFe_2O_4$/F@C consists of C, F, Mn, Fe and O elements. The F-element mapping image overlaps with those of Mn, Fe and O, thus confirming that the $MnFe_2O_4$ nanorods are successfully doped with fluoride. Moreover, we can see that C, F, Mn, Fe and O elements are evenly distributed over the whole image, which proves that the $MnFe_2O_4$/F nanorods are homogeneously dispersed in the carbon matrix.

More detailed structural characteristics for the as-prepared nanorod-$MnFe_2O_4$/F@C were determined by a TEM and SAED pattern analysis. The TEM image (Fig. 6a) indicates that the as-prepared nanorod-$MnFe_2O_4$/F@C with numerous porous structures is wrapped by carbon layers. The corresponding HRTEM image obtained from the edge of nanorod-$MnFe_2O_4$/F@C (Fig. 6c) shows clear lattice fringes, revealing the high crystallinity of the sample.

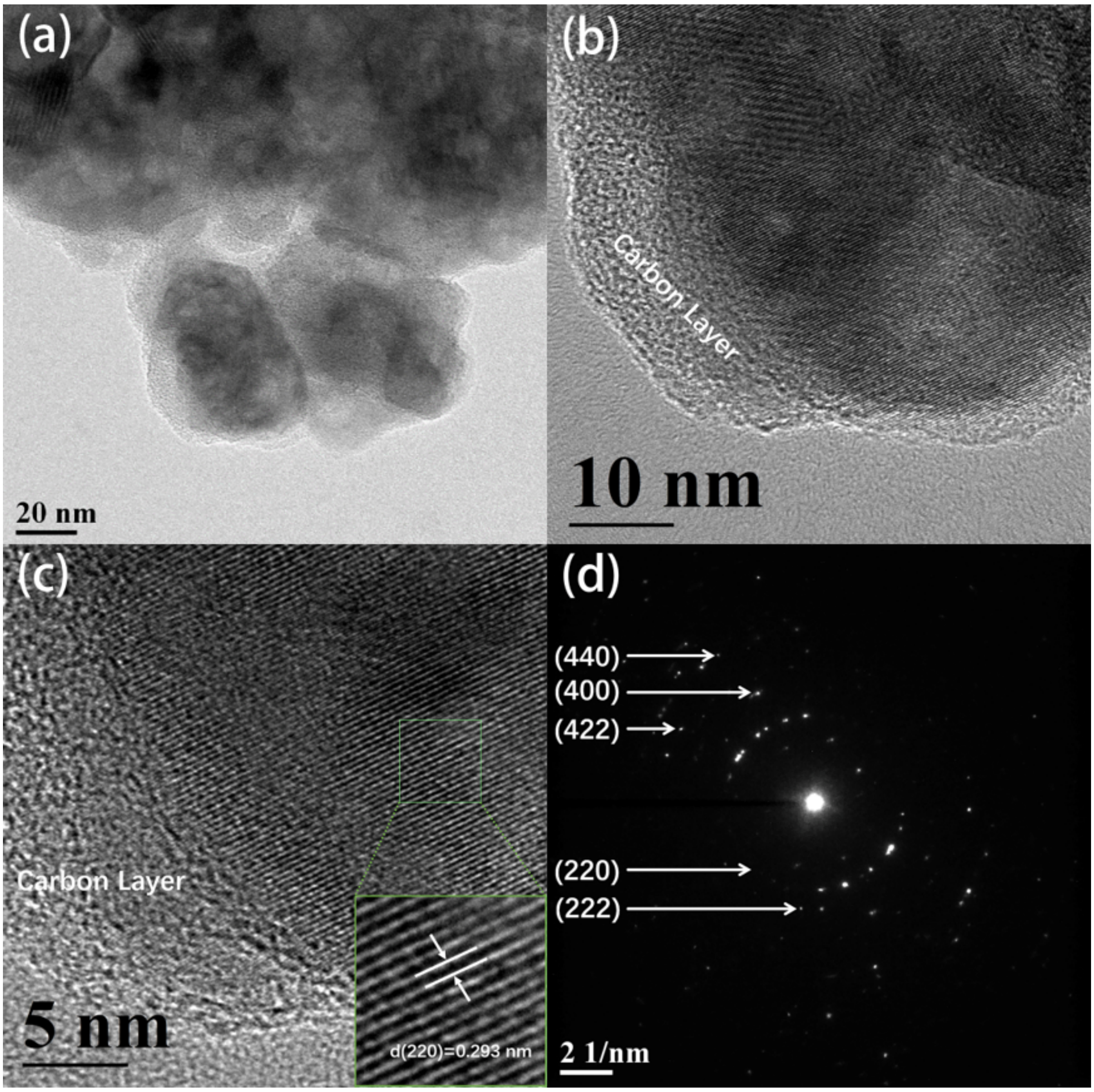

Figure 6. (a) Low-magnification TEM image, (b, c) HRTEM images of nanorod-$MnFe_2O_4$/F@C and the (d) SAED pattern of nanorod-$MnFe_2O_4$/F@C.

The lattice interplanar spacings are measured to be 0.293 nm, which is in accordance with the *d*-spacings of the (2 2 0) crystal planes of $MnFe_2O_4$ (JCPDS No. 74-2403). Moreover, it is obvious from the HRTEM images that the $MnFe_2O_4$ nanorods are coated by the carbon layers (Fig. 6b, c), further confirming the successful wrapping of the carbon layers on the $MnFe_2O_4$ nanorods. The carbon layers can effectively buffer the volume variation of the $MnFe_2O_4$ nanorods during the Li-ion insertion/extraction process. In addition, the SAED pattern (Fig. 6d) shows a set of well-defined diffraction spots of the as-prepared $MnFe_2O_4$ nanorods. All the diffraction spots can be well indexed as a cubic spinel $MnFe_2O_4$ phase and are consistent with the XRD pattern. The SAED pattern also indicates ~~that~~ the polycrystalline nature of the $MnFe_2O_4$ nanorods.

Cyclic voltammetry (CV) measurements were used to analyse the redox reaction mechanism. Fig. 7a shows the CV curves of nanorod-$MnFe_2O_4$/F@C for the first three cycles at a scan rate of 0.1 mV s^{-1} and in a range of 0.01-3.0 V.

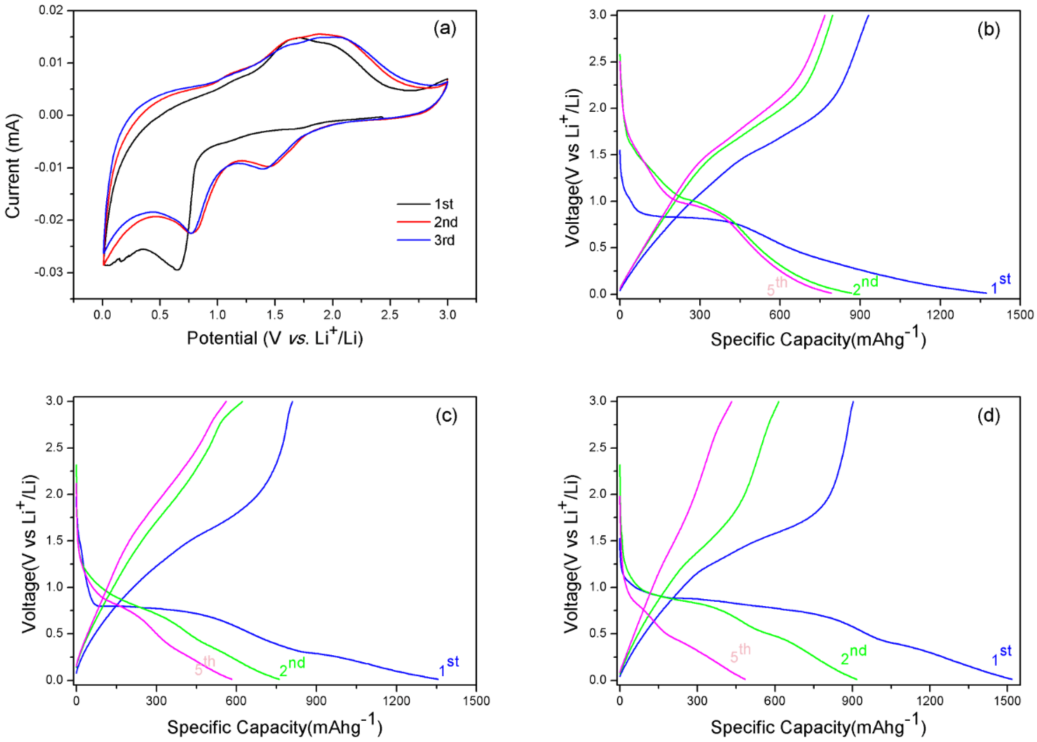

Figure 7. (a) Cyclic voltammograms of nanorod-$MnFe_2O_4$/F@C for the first three cycles at a scan rate of 0.1 mVs^{-1} and in a range of 0.01-3.0 V. The charge-discharge curves of (b) nanorod-$MnFe_2O_4$/F@C, (c) nanorod-$MnFe_2O_4$@C, and (d) pure nanorod-$MnFe_2O_4$ after the 1st, 2nd, and 5th cycles between 0.01 V and 3 V at a current density of 200mA g^{-1}.

In the first cathodic scan, a broad peak located at approximately 0.65 V can be attributed to the reduction of $MnFe_2O_4$ to Mn^0 and Fe^0 as well as the formation of Li_2O and SEI films [24, 57]. In the subsequent cathodic scan, the main peaks are positively shifted, which is due to a lattice structure rearrangement of $MnFe_2O_4$ and corresponds to the reduction of MnO to Mn and Fe_3O_4 to Fe. The relatively small peaks appearing at 1.5 V in the subsequent cathodic scan can be attributed to the Faradaic capacitance [58]. In the first anodic scan, the main peak located at 1.7 V corresponds to the oxidation of Mn to MnO and Fe to Fe_3O_4, respectively. In the subsequent cycles, the main anodic peaks are positively shifted because of the polarization of the electrode materials [59,60]. Reversible redox reactions between MnO/Fe_3O_4 and Li_2O/Mn/Fe occur after the first cathodic scan. Compared with the first cathodic scan, the integrated area of the subsequent cathodic scan is decreased due to electrode pulverization, electrolyte decomposition, and the formation of an SEI film. After the first cycle, the integrated areas remain almost unchanged, indicating that the electrodes possess high stability and reversibility for Li-ion storage. The electrochemical performance of nanorod-$MnFe_2O_4$/F@C was evaluated by galvanostatic charge and discharge measurements at a current density of 200 mA g^{-1} and in a voltage range 0.01-3 V vs Li^+/Li, as shown in Fig. 7b. For comparison, the discharge and charge curves of nanorod-$MnFe_2O_4$/F@C and bare nanorod-$MnFe_2O_4$ are also shown in Fig. 7c and Fig. 7d. In the case of nanorod-$MnFe_2O_4$/F@C, the first charge and discharge capacities are 932 and 1372 mA h g^{-1}, respectively, showing an initial coulombic efficiency of 68%. The relatively high irreversible capacity loss is mainly attributed to electrolyte decomposition and the formation of the SEI film [18, 59, 60]. Furthermore, the coulombic efficiency reaches 97% after the 5th cycle and remains stable in subsequent cycles. However, the discharge capacity of nanorod-$MnFe_2O_4$/F@C and bare nanorod-$MnFe_2O_4$ shows a rapid decrease in the initial five cycles.

The first discharge curves of nanorod-$MnFe_2O_4$/F@C show a clear voltage plateaus at 0.8 V which can be described as the following reaction [59]:

$$\mathrm{MnFe_2O_4 + 8Li^+ + 8e^- \rightarrow Mn + 2Fe + 4Li_2O}$$

The plateaus are in accordance with other reports [45,46], followed by a long sloping curve to a cut-off voltage of 0.01 V. After the first discharge process, the discharge potential plateau is replaced by a long slope between 1.1 V and 0.8 V and a charge plateau between 1.5 V and 2 V remains stable. These voltage plateaus are formed owing to the reversible oxidation and reduction reactions between MnO/Fe_3O_4 and Mn/Fe during the Li-ion insertion/extraction process.

The reversible redox reaction is described as follows:

$$\mathrm{Mn + 3Fe + 5Li_2O \leftrightarrow MnO + Fe_3O_4 + 10Li^+ + 10e^-}$$

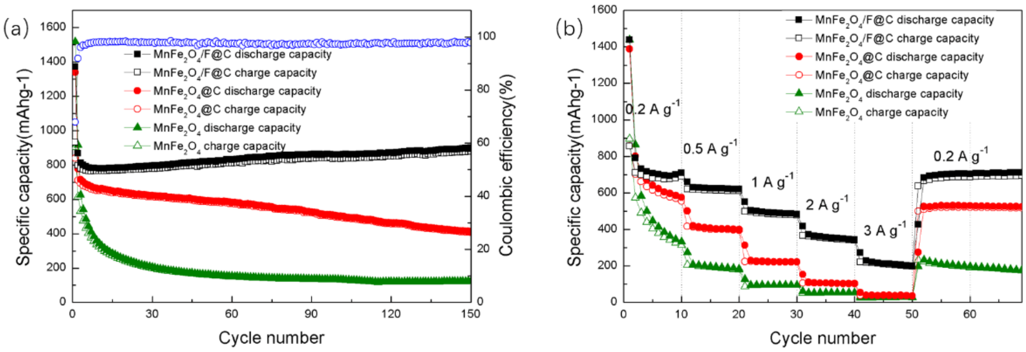

Figure 8. (a, b) Cycling performance and rate performance of nanorod-$MnFe_2O_4$/F@C, nanorod-$MnFe_2O_4$@C, and pure nanorod-$MnFe_2O_4$ at a current density of 200 mA g^{-1}

Fig. 8a compares the cycling performance of nanorod-$MnFe_2O_4$/F@C, nanorod-$MnFe_2O_4$@C and nanorod-$MnFe_2O_4$ at a current density of 200 mA g^{-1} in a voltage range of 0.01-3 V vs. Li^+/Li. The significant enhancement of electrochemical performance with the introduction of fluoride can be observed from the excellent cycling stability of the nanorod-$MnFe_2O_4$/F@C. Furthermore, as a result of the irreversible capacity loss caused by the formation of the SEI film and other side reactions, nanorod-$MnFe_2O_4$/F@C experiences a significant capacity decrease in the initial discharge process [61]. Although the discharge specific capacity of ~~the~~ nanorod-$MnFe_2O_4$/F@C decreases with increasing cycle number in the first 10 cycles, the discharge specific capacity becomes stable and increases slowly for the rest of the cycles. After 150 cycles, nanorod-$MnFe_2O_4$/F@C is still able to deliver a discharge specific capacity of 900 $mAhg^{-1}$, which is significantly higher than that of pure nanorod-$MnFe_2O_4$ (125 mAhg^{-1}) and nanorod-$MnFe_2O_4$@C (412 mAhg^{-1}). The Coulombic efficiency of nanorod-$MnFe_2O_4$/F@C quickly reaches ~98% and is retained after 150 cycles. Nanorod-$MnFe_2O_4$/F@C demonstrates better cycling performance because the introduction of fluoride can enhance the electrical conductivity and structural stability of the electrode [35].

Table 1. Electrochemical performance comparison of $MnFe_2O_4$-based anodes for lithium-ion batteries.

Materials	Current density (mA g^{-1})	Cycle number	Capacity (mA h g^{-1})	Refs.
Porous $MnFe_2O_4$/ RGO nanocomposites	92.8	30	905	[63]
$MnFe_2O_4$/ RGO nanocomposite	200	100	653	[30]
$MnFe_2O_4$/ RGO nanocomposite	1000	200	581	[64]
$MnFe_2O_4$/graphene composites	200	80	684	[65]
Carbon-coated $MnFe_2O_4$ hollow microspheres	200	100	970	[41]
Porous $MnFe_2O_4$ microrods	100	1000	630	[66]
Carbon-coated $MnFe_2O_4$ nanospheres	100	50	646	[65]
Nanorod-$MnFe_2O_4$/F@C	200	150	900	This work

For comparison, the cycling performance of other previously reported pure $MnFe_2O_4$ or $MnFe_2O_4$-based anode materials is listed in Table 1. The table demonstrates that nanorod-$MnFe_2O_4$/F@C exhibits better or comparable electrochemical performance compared to that of most $MnFe_2O_4$-based anode materials. Fig. 8b compares the rate performance of nanorod-$MnFe_2O_4$/F@C, nanorod-$MnFe_2O_4$@C and pure nanorod-$MnFe_2O_4$ at different current densities. Nanorod-$MnFe_2O_4$/F@C exhibits high stability and high discharge capacities of 710, 630, 490, 360 and 220 mA h g^{-1} at ~~the~~ current densities of 200, 500, 1000, 2000 and 3000 mA g^{-1}, respectively. Moreover, when the current densities return to 200 mA g^{-1}, the discharge capacity returns to 705 mA h g^{-1} after 10 cycles. In subsequent cycles, the capacity of nanorod-$MnFe_2O_4$/F@C shows a slow but continuous increase. For comparison, the capacity of nanorod-$MnFe_2O_4$@C and pure nanorod-$MnFe_2O_4$ decreases rapidly with increasing current density. Nanorod-$MnFe_2O_4$@C shows a high stability and high capacity at different current densities compared with that of pure nanorod-$MnFe_2O_4$ which can be attributed to the incorporation of carbon. The carbon has superior electron and ion conductivity, excellent buffering capability and outstanding structural stability during Li ion insertion and extraction process. However, the rate performance of nanorod-$MnFe_2O_4$@C is still worse than that of nanorod-$MnFe_2O_4$/F@C. The reason for this phenomenon may be attributed to the doped fluorine because fluorine-doped metal oxides have enhanced electrochemical performance [38, 51, 62] and can suppress the decomposition of the electrolyte; thus, fluorine doping leads to the formation of a thick solid electrolyte interphase (SEI) film, and eventually, an enhanced cycling stability of the anode material.

4. CONCLUSIONS

In summary, ~~a~~ fluorine-doped MnFe2O4 nanorods and carbon nanocomposites (nanorod-$MnFe_2O_4$/F@C) were successfully synthesized by a simple and facile hydrothermal reaction followed by a subsequent calcination process using glucose as a carbon source. The nanorod-$MnFe_2O_4$/F@C shows enhanced cycling and rate performance compared to those of the MnFe2O4 nanorods and carbon nanocomposite (nanorod-$MnFe_2O_4$@C) without the addition of ammonium fluoride. The excellent capacity retention and high discharge capacity of nanorod-$MnFe_2O_4$/F@C is due to the nanorod structure, which provides a large specific surface area, more active sites and fast lithium and electron diffusion pathways for Li ion storage. The presence of carbon is beneficial for improving electron and ion conductivity and alleviating volume variation during Li ion insertion and extraction processes. The above strategies are green and suitable for large-scale industrial production and it is anticipated that nanorod-$MnFe_2O_4$/F@C will be a promising anode material for next generation Li-ion batteries.

ACKNOWLEDGEMENTS
This work was supported by the National Natural Science Foundation of China (Grant no.61875187).

References

1. J. Maier, *Nat. Mater.,* 4 (2005) 805.
2. J.B. Goodenough, K.S. Park, *J. Am. Chem. Soc.,* 135 (2013) 1167.
3. Y. Guo, J. Hu, L. Wan, *Adv. Mater.,* 20 (2008) 2878.
4. S. Goriparti, E. Miele, F. De Angelis, E. Di Fabrizio, R. Proietti Zaccaira, C. Capiglia, *J. Power Sources,* 257 (2014) 421.
5. J.M. Tarascon, M. Armand, *Nature,* 414 (2001) 359.
6. Y. Zhong, H. Fan, L. Chang, H. Shao, J. Wang, J. Zhang, C. Cao, *J. Power Sources,* 296 (2015) 255.
7. J. Zhang, A. Yu, *Chin. Sci. Bull.,* 60 (2015) 823.
8. G. Zhang, Y. Shi, H. Wang, L. Jiang, X. Yu, S. Jing, S. Xing, P. Tsiakaras, *J. Power Sources,* 416 (2019) 118.
9. W. Xiong, Y. Jiang, Y. Xia, Y. Qi, W. Sun, C. Hu, R. He, B. Chen, Y. Liu, X. Zhao, *J. Power Sources,* 401 (2018) 65.
10. Y. Li, B. Tan, Y. Wu, *Nano Lett.,* 8 (2008) 265.
11. X. Lou, D. Deng, J. Lee, J. Feng, L.A. Archer, *Adv. Mater.,* 20 (2008) 258.
12. L. Li, C. Nan, J. Lu, Q. Peng, Y. Li, *Chem. Commun.,* 48 (2012) 6945.
13. D. Yan, P.X. Yan, G.H. Yue, J.Z. Liu, J.B. Chang, Q. Yang, D.M. Qu, Z.R. Geng, J.T. Chen, G.A. Zhang, R.F. Zhuo, *Chem. Phys. Lett.,* 440 (2007) 134.
14. Z. Favors, W. Wang, H.H. Bay, A. George, M. Ozkan, C.S. Ozkan, *Sci. Rep.,* 4 (2014) 4605.
15. T. He, J. Feng, Y. Zhang, L. Zu, G. Wang, Y. Yu, J. Yang, *Adv. Energy Mater.,* 8 (2018) 1702805.
16. Z. Wen, G. Lu, S. Mao, H. Kim, S. Cui, K. Yu, X. Huang, P.T. Hurley, O. Mao, J. Chen, *Electrochem. Commun.,* 29 (2013) 67.
17. C. Yuan, H. Wu, Y. Xie, X. Lou, *Angew. Chem. Int. Ed.,* 53 (2014) 1488.
18. Y. Wang, D. Su, A. Ung, J. Ahn, G. Wang, *Nanotechnology,* 23 (2012) 055402.
19. H. Xia, D. Zhu, Y. Fu, X. Wang, *Electrochim. Acta,* 83 (2012) 166.
20. Z. Yang, Y. Huang, J. Hu, L. Xiong, H. Luo, Y. Wan, *Synth. Met.,* 242 (2018) 92.
21. J. Sui, C. Zhang, D. Hong, J. Li, Q. Cheng, Z. Li, W. Cai, *J. Mater. Chem.,* 22 (2012) 13674.
22. M. Yu, Y. Huang, K. Wang, X. Han, M. Wang, Y. Zhu, L. Liu, *Appl. Surf. Sci.,* 462 (2018) 955.
23. J. Xie, W. Song, G. Cao, T. Zhu, X. Zhao, S. Zhang, *RSC Adv.,* 4 (2014) 7703.
24. Y. Xiao, J. Zai, L. Tao, B. Li, Q. Han, C. Yu, X. Qian, *Phys. Chem. Chem. Phys.,* 15 (2013) 3939.

25. W. Zhang, X. Hou, Z. Lin, L. Yao, X. Wang, Y. Gao, S. Hu, *J. Mater. Sci. – Mater. Electron.,* 26 (2015) 9535.
26. S. Li, B. Wang, B. Li, J. Liu, M. Yu, X. Wu, *Mater. Res. Bull.,* 61 (2015) 369.
27. C. Zhang, C. Jin, G. Teng, Y. Gu, W. Ma, *Chem. Eng. J.,* 365 (2019) 121.
28. P. Lavela, J.L. Tirado, *J. Power Sources,* 172 (2007) 379.
29. S. Bourrioux, L.P. Wang, Y. Rousseau, P. Simon, A. Habert, Y. Leconte, M.T. Sougrati, L. Stievano, L. Monconduit, Z.J. Xu, M. Srinivasan, A. Pasturel, *New J. Chem.,* 41 (2017) 9236.
30. K. Wu, G. Hu, Y. Cao, Z. Peng, K. Du, *Mater. Lett.,* 161 (2015) 178.
31. L. Yang, L. Liu, Y. Zhu, X. Wang, Y. Wu, *J. Mater. Chem.,* 22 (2012) 13148.
32. Q. Sun, M. Bijelić, A.B. Djurišić, C. Suchomski, X. Liu, M. Xie, A.M.C. Ng, H. Kong Li, K. Shih, S. Burazer, Ž. Skoko, I. Djerdj, J. Popović, *Nanotechnology,* 28 (2017) 455401.
33. M.W. Forney, M.J. Ganter, J.W. Staub, R.D. Ridgley, B.J. Landi, *Nano Lett.,* 13 (2013) 4158.
34. H. Liu, W. Li, D. Shen, D. Zhao, G. Wang, *J. Am. Chem. Soc.,* 137 (2015) 13161.
35. J. Sun, L. Xiao, S. Jiang, G. Li, Y. Huang, J. Geng, *Chem. Mater.,* 27 (2015) 4594.
36. S. Huang, Y. Li, Y. Feng, H. An, P. Long, C. Qin, W. Feng, *J. Mater. Chem. A,* 3 (2015) 23095.
37. C. Wang, Y. Zhang, Y. Li, J. Liu, Q. Wu, J. Jiang, Y. Li, J. Lu, *Nanotechnology,* 28 (2017) 065401.
38. K. Karthikeyan, S. Amaresh, S.N. Lee, V. Aravindan, Y.S. Lee, *Chem. Asian J.,* 9 (2014) 852.
39. H. Geng, H. Ming, D. Ge, J. Zheng, H. Gu, *Electrochim. Acta,* 157 (2015) 1.
40. Z. Wu, L. Xue, W. Ren, F. Li, L. Wen, H. Cheng, *Adv. Funct. Mater.,* 22 (2012) 3290.
41. Y. Yan, G. Guo, T. Li, D. Han, J. Zheng, J. Hu, D. Yang, A. Dong, *Electrochim. Acta,* 246 (2017) 43.
42. C. Zhang, Z. Mo, G. Teng, B. Wang, R. Guo, P. Zhang, *J. Mater. Chem. B.,* 1 (2013) 5908.
43. T. Wu, Y. Liu, X. Zeng, T. Cui, Y. Zhao, Y. Li, G. Tong, *Acs Appl. Mater. Interfaces,* 8 (2016) 7370.
44. C. He, S. Wu, N. Zhao, C. Shi, E. Liu, J. Li, *ACS Nano,* 7 (2013) 4459.
45. Q. Wang, B. Wang, Z. Zhang, Y. Zhang, J. Peng, Y. Zhang, H. Wu, *Inorg. Chem. Front.,* 5 (2018) 2605.
46. J. Zhu, T. Zhu, X. Zhou, Y. Zhang, X. Lou, X. Chen, H. Zhang, H.H. Hng, Q. Yan, *Nanoscale,* 3 (2011) 1084.
47. G. Wang, X. Shen, J. Yao, J. Park, *Carbon,* 47 (2009) 2049.
48. H. Xia, Y. Wan, G. Yuan, Y. Fu, X. Wang, *J. Power Sources,* 241 (2013) 486.
49. U. Byambasuren, Y. Jeon, D. Altansukh, Y.-G. Shul, *J. Solid State Electrochem.,* 20 (2015) 645.
50. N. Huo, Y. Yin, W. Liu, J. Zhang, Y. Ding, Q. Wang, Z. Shi, S. Yang, *New J. Chem.,* 40 (2016) 7068.
51. J. Hu, R.G. Gordon, *Sol. Cells,* 30 (1991) 437.
52. G.G. Amatucci, N. Pereira, T. Zheng, J.M. Tarascon, *J. Electrochem. Soc.,* 148 (2001) 171.
53. Y. Yao, Y. Cai, F. Lu, F. Wei, X. Wang, S. Wang, *J. Hazard. Mater.,* 270 (2014) 61.
54. H. Kim, D. Seo, H. Kim, I. Park, J. Hong, K. Park, K. Kang, *Chem. Mater.,* 24 (2012) 720.
55. X. Zhu, Y. Zhu, S. Murali, M.D. Stoller, R.S. Ruoff, *ACS Nano,* 5 (2011) 3333.
56. C. Pereira, A.M. Pereira, P. Quaresma, P.B. Tavares, E. Pereira, J.P. Araujo, C. Freire, *Dalton Trans.,* 39 (2010) 2842.
57. P. Balaya, H. Li, L. Kienle, J. Maier, *Adv. Funct. Mater.,* 13 (2003) 621.
58. Y.J. Mai, D. Zhang, Y.Q. Qiao, C.D. Gu, X.L. Wang, J.P. Tu, *J. Power Sources,* 216 (2012) 201.
59. S. Liu, J. Xie, Q. Su, G. Du, S. Zhang, G. Cao, T. Zhu, X. Zhao, *Nano Energy,* 8 (2014) 84.
60. P. Poizot, S. Laruelle, S. Grugeon, L. Dupont, J.M. Tarascon, *J. Power Sources,* 97 (2001) 235.
61. C. Xu, Y. Zeng, X. Rui, N. Xiao, J. Zhu, W. Zhang, J. Chen, W. Liu, H. Tan, H.H. Hng, Q. Yan, *ACS Nano,* 6 (2012) 4713.
62. G.G. Amatucci, N. Pereira, *J. Fluorine Chem.,* 128 (2007) 243.
63. P. Kollu, P.R. Kumar, C. Santosh, D.K. Kim, A.N. Grace, *RSC Adv.,* 5 (2015) 63304.
64. H. Tang, P. Gao, A. Xing, S. Tian, Z. Bao, *RSC Adv.,* 4 (2014) 28421.

65. F. Jiang, X. Du, S. Zhao, J. Guo, B. Huang, X. Huang, Q. Su, J. Zhang, G. Du, *J. Nanopart. Res.,* 17 (2015) 173.
66. N. Wang, X. Ma, Y. Wang, J. Yang, Y. Qian, *J. Mater. Chem. A.,* 3 (2015) 9550.